K.P. Geigle, R. Hadef, M. Stöhr, W. Meier, Flow field characterization of pressurized sooting swirl flames and correlation to soot distributions, Proc. Combustion Institute 36 (2017) 3917-3924.

The original publication is available at www.elsevier.com

http://dx.doi.org/10.1016/j.proci.2016.09.024

Flow field characterization of pressurized sooting swirl flames and relation to soot distributions

Klaus Peter Geigle[1], Redjem Hadef[2], Michael Stöhr[1], Wolfgang Meier[1]

[1] Deutsches Zentrum für Luft- und Raumfahrt e.V.
Institut für Verbrennungstechnik
Pfaffenwaldring 38-40
D-70569 Stuttgart (Germany)
klauspeter.geigle@dlr.de
Tel. +49-711-6862 398
Fax +49-711-6862 578

[2] Université Larbi Ben M'Hidi
Institut de Génie Mécanique
04000 Oum El Bouaghi (Algerie)

Colloquium:	Gas Turbines (IC Engine and Gas Turbine Combustion)
First alternate colloquium:	Soot
Second alternate colloquium:	Diagnostics

Length of Paper – Based on Method 1

Text:

Main Text:	4198 words Including Introduction, Body, Conclusions, and Acknowledgments.
References:	437 words (23 references + 2) x (2.3 lines/reference) x (7.6 words/line)
Table:	137 words (3 text lines + 2 lines) x (7.6 words/line) x (2 columns)

Figures:

Figure 1: (49 + 10)mm × (2.2 words/mm) × (1 column) + (25 words in caption)
= 155 Words
Figure 2: (63 + 10)mm × (2.2 words/mm) × (2 column) + (40 words in caption)
= 361 Words
Figure 3: (58 + 10)mm × (2.2 words/mm) × (2 column) + (45 words in caption)
= 195 Words
Figure 4: (38 + 10)mm × (2.2 words/mm) × (1 column) + (14 words in caption)
= 120 Words
Figure 5: (53.7 + 10)mm × (2.2 words/mm) × (1 column) + (32 words in caption)
= 312 Words
Figure 6: (46.5 + 10)mm × (2.2 words/mm) × (1 column) + (37 words in caption)
= 286 Words

Total Word Count: 4198 + 437 + 137 + 155 + 361 + 195 + 120 + 312 + 286
= 6200 Words (limit is 6200 words)

Abstract

Mean and instantaneous flow fields were derived for sooting pressurized swirl flames, operated with ethylene/air in an aero-engine model combustor. Stereo particle image velocimetry served to deduce three velocity components and to identify locations of soot based on soot scattering. The measurements complement those of other quantities in the same flames published recently. Flow fields determined for cold and reactive conditions confirm conclusions drawn from application of other laser-based diagnostics: soot is mainly formed in the inner recirculation zone which recirculates reactive, hot unburnt reaction products, and partly transported into the high-velocity in-flow regions. Oxidation air injected after two thirds of the combustor forms a stagnation zone close to the combustor axis and splits into a portion flowing downstream towards the combustor exit and one transported upstream thereby affecting the local gas composition and temperatures in the inner recirculation zone. Analysis of the instantaneous images by proper orthogonal decomposition reveals the existence of a precessing vortex core which impacts the soot distribution. Presence of soot in high-velocity/high strain rate regions where soot formation is unlikely to occur can be explained as a result of transport. Flow field characterization and the correlation with soot presence, in complement of existing data, are expected to provide a valuable contribution to soot model validation.

Keywords: soot, flow field, gas turbine, model combustor, pressure

1. Introduction

Expected more stringent emission legislation for kerosene combustion in aero-engines has driven considerable effort in recent years to better understand, model and predict soot formation in gas turbine combustors. Increasingly, numerical tools contribute to the understanding of processes leading to soot formation and oxidation in technical combustors [1,2]. Yet experiments remain essential to improve the predictive capability of soot modelling. Those can either serve to improve understanding of fundamental sub-processes such as soot inception, growth, and oxidation, as well as soot-turbulence interaction, or as validation data for numerical models. Numerous studies in fundamental flames exist; however, there is an increasing need for data sets

derived from flames which exhibit technical features such as pressure, turbulence and swirl. Those data sets should preferably include soot and temperature, and beyond that as many quantities as possible. A combination of both, technical conditions at well-defined boundary conditions, and detailed characterization by accurate optical diagnostics, remains challenging. Recently, we presented a series of publications characterizing such a semi-technical combustor which exhibits the mentioned technical features [3-5]. It also offers the option to inject additional oxidation air downstream of the primary combustion zone which mimics dilution or quench air as employed in aero-engine combustors. The data set includes mean and instantaneous distributions of soot, OH and PAH as well as temperatures measured by laser-induced incandescence (LII), laser-induced fluorescence (LIF) and coherent anti-Stokes Raman scattering (CARS). In addition, correlations exist where two complementary techniques were applied simultaneously. The current study adds information on the velocity field which is important for several reasons: soot formation depends strongly on local gas composition, temperature and the time history of the respective fluid element. The instantaneous flow field is an essential quantity impacting those parameters via turbulent mixing. Resulting quantities as residence times, velocity gradients (strain) and dissipation contribute to the local thermochemical state which eventually leads to soot formation or oxidation of precursors prior to forming soot [6-8]; high strain rates reduce the formation of soot precursors PAH (polycyclic aromatic hydrocarbons [7]), and consequently soot. Turbulent fluctuations impacting these mentioned pathways therefore directly result in the strong soot intermittency determined in turbulent flames (for example [9-12]). The direct correlation of flow field and soot distribution, however, is further complicated by the different time scales of soot chemistry and turbulence. Soot chemistry is typically described as a relatively slow process on the order of several milliseconds (for example [13-15]). Dependent on the location in the flame, time scales of the flow field cover a significantly wider range from sub-milliseconds close to the flame front to multiple milliseconds in the inner recirculation zone, which rather would require a time-resolved determination of the correlation of soot and flow field. However, for combustion simulation the non-reacting, and subsequently reacting flow fields are the first quantities to validate turbulence modeling prior to employing chemistry modules. Application of particle image velocimetry (PIV) to sooting flames is challenging due to strong flame luminosity, and the number of publications showing application of PIV to sooting flames for validation purposes is limited (for example [8,16,17]). The focus of this work is to complement the existing data set with mean velocity distributions and

statistics, and provide additional insight into processes related to soot formation in complex flames by correlating soot distributions to the flow field.

2. Setup

2.1. Burner

The burner used in this study has been presented in detail in a recent publication [4] and is only briefly described here. The injector consists of a pair of annular air swirl nozzles separated by a ring of 60 tiny fuel-injection channels (0.5x0.4 mm^2). Ethylene is introduced through these inlets, the central air outlet has a diameter of 12.3 mm and the outer air nozzle measures 19.8 mm. The combustion chamber has a square cross section of 68x68 mm^2 and is 120 mm long. The water-cooled metal posts holding the quartz windows, which serve for good optical access, have an additional air duct of 5 mm inner diameter allowing injection of additional oxidation air after two thirds of the combustor. The four radially-injected jets meet on the combustor axis and form a stagnation zone. The water-cooled top plate of the combustion chamber has a cylindrical exhaust hole (diameter 40 mm, length 24 mm), linked to the combustion chamber by a curvature. 3-mm-thick quartz windows allow for excellent optical access to the flame. Both combustion air flows are supplied by separate mass flow controllers. Those, and controllers for fuel and oxidation air (Bronkhorst) were calibrated in-house resulting in an accuracy of clearly better than 1% of the maximum flow.. All fluids are injected at ambient temperature.

The combustor is mounted in a water-cooled steel pressure housing with large optical access (60×120 mm^2) from four sides. The pressure can be adjusted by partially blocking the exhaust port with a movable piston. An air flow through the gap between the combustion chamber and the pressure housing serves as air cooling for the windows of the combustion chamber.

Among the operating conditions characterized recently by other diagnostics, two were specifically selected for the current study (table 1). Primarily, this is the so-called reference point at 3 bar, ϕ=1.2, with 40% additional oxidation air and 30% of the combustion air passing through the central air nozzle, 70% through the annular air passage. This operating point was characterized without combustion, yet fuel present, with and without additional oxidation air, as well as with combustion. In addition, a leaner case at ϕ=0.9 of lower soot content,

and less luminosity, was studied enabling a detailed data analysis including correlations of instantaneous soot distributions with velocity fields. For both conditions the full suite of optical diagnostics has been applied recently to determine OH, PAH and quantitative soot distributions as well as temperature statistics. The current study was limited to those two cases because most other flames of the full series of validation flames [3] exhibited stronger soot luminosity and thus were even more challenging than those two investigated here.

Table 1. Flame parameters for studied flames: Pressure, p, flow rates for air through burner (central and ring), $Q_{air,c}$, and $Q_{air,r}$, fuel, Q_{fuel}, oxidation air through secondary air inlet, Q_{oxi}, equivalence ratios, ϕ, ϕ_{global}, thermal powers, P, P_{global}, and ratios $Q_{air,c}/Q_{air}$ and Q_{oxi}/Q_{air} with $Q_{air}=Q_{air,c}+Q_{air,r}$. Flow rates in standard liters per minute (slm) are referenced to 1.013 bar and 273 K.

p [bar]	ϕ	$P_{primary}$ [kW]	$Q_{air,c}$ [slm]	$Q_{air,r}$ [slm]	Q_{fuel} [slm]	Q_{oxi} [slm]	$\frac{Q_{air,c}}{Q_{air}}$	$\frac{Q_{oxi}}{Q_{air}}$	ϕ_{global}	P_{global} [kW]
3	0.9	32.2	156.0	365.1	32.7	208.2	0.3	0.4	0.64	32.2
3	1.2	32.2	140.8	328.5	39.3	187.4	0.3	0.4	0.86	38.6

2.2. Particle Image Velocimetry and Derivation of Soot Distributions

Stereo PIV was applied in this study because validation data in swirl flames essentially need to include the tangential velocity component. To capture most of the flame we mounted the pair of CCD cameras as close as possible to the pressure flange of the high-pressure housing and employed wide-angle lenses.

Three-component velocity fields were measured using a stereoscopic PIV system (FlowMaster, LaVision). The system consisted of a frequency-doubled dual-head Nd:YAG laser (NewWave Solo 120), a programmable timing unit (PTU, LaVision) and two double-shutter CCD cameras (Imager ProX, 1600×1200 pixels, LaVision) equipped with a 532 nm bandpass filter of either 11 nm or 1 nm bandwidth (FWHM) to block the majority of the soot luminosity. The 1 nm filter provided a better suppression of soot luminosity, but resulted in a relatively small field of view (FoV) due to its low transmission at non-perpendicular incident angles. The laser was operated with an energy of 120 mJ per pulse at 532 nm and a repetition rate of 5 Hz.

The laser beam was expanded to a 100 mm tall planar light sheet that covered the central vertical section of the combustion chamber. The thickness of the light sheet was around 1 mm. Scheimpflug adapters were mounted such that the focal planes of the cameras coincide with the laser sheet. The two cameras were located as close as possible to the combustor in order to achieve a relatively large stereoscopic angle. In the present configuration, the distance between the camera lenses (f=16 mm, f/4–f/16) and the measurement plane was

approximately 150 mm (i.e. the cameras were almost touching the window flange), resulting in a stereoscopic viewing angle of approximately 37°. For calibration of the camera system we used a 3D calibration plate (LaVision Type 11).

The three air flows (central and ring combustion air, oxidation air) were seeded with TiO_2 particles with a nominal diameter of 1 µm. Due to contamination of combustor windows with seed particles, the duration of measurements was limited to about 10 and 30 minutes at reacting and non-reacting conditions, respectively. Thereafter the combustor had to be shut down and windows had to be cleaned before further measurements could be performed.

From the raw particle images, the soot and flame luminosity was removed by subtracting background images determined with both spatial and temporal sliding median filters. Velocity fields were then calculated using commercial PIV software (DaVis 8, LaVision). A multi-scale cross-correlation algorithm was used with a final interrogation window size of 32×32 or 16×16 pixel, corresponding to an in-plane spatial resolution of 3.4×3.4 or 1.7×1.7 mm². Spurious vectors were detected using the deviation from the local median, and replaced either by vectors corresponding to the 2nd, 3rd or 4th highest correlation peak (if they fulfil the median criterion), or otherwise by an interpolated vector. The commercial software also served to derive extensive strain rate distributions.

Measurements were performed in two sequences: in a first iteration the non-reacting flow field was recorded for identical flow rates (including fuel) and pressure as for the reacting test cases. The second iteration consisted of application to the respective flames. To cope with the relatively strong soot luminosity emitted by the reference flame at ϕ=1.2 we followed two different detection schemes: use of 2-nm wide narrowband filters which reduced the field of view to approximately 50 mm diameter and therefore required vertical translation of the cameras to capture a large enough part of the combustor. The second scheme used 10-nm wide filters. The latter results in a sum-of-correlation (SoC) mean velocity information [18,19], which allows mapping of the whole combustor for a global impression of the flow field but does not yield statistical information.

The PIV images suffer from soot presence in two respects: due to the system-inherent long exposure times the second camera frame accumulates significant line-of-sight integrated soot luminosity, which for luminous

flames can outshine scatter signal from PIV seed particles and lead to camera saturation. In addition to luminosity, Rayleigh scattering from soot particles adds to the scatter by PIV seed. By adequate image processing we made use of this effect and derived instantaneous soot distributions from the first PIV frames. A sliding minimum subtraction (identification of suitable parameterization required) removes the image background and distributed signal from irradiated surfaces. This is followed by application of a linear erosion filter to remove seed particle scatter and leaves the soot structures, as verified by simultaneously measured LII. As the main purpose of this study was a spatial correlation of soot presence with the instantaneous flow field, we rather used this, instead of available LII images which were recorded upon LII excitation by the first PIV laser pulse. The use of the identical camera to derive flow field and soot presence facilitated spatial overlap and correlations. Also, image intensifier smear, which deteriorates the resolution in LII, was not an issue here. Note that soot quantification has been presented recently [3], and was not topic of the current study. Suitability of the PIV-camera-derived soot distributions was verified using the LII images though.

3. Results

3.1. Non-Reacting Flow Field

Fig. 1 visualizes the mean velocity distribution of the cold flow for the reference case (right) and the same case without injection of additional oxidation air at x=80 mm (left). Color denotes the tangential velocity component v_z, the arrows describe the in-plane motion, the dashed contour represents the v_y=0 m/s isoline. Both cases exhibit the major characteristics of injectors used for swirl stabilized flames: a relatively high-velocity in-flow, a pronounced inner recirculation zone (IRZ) and an outer recirculation zone (ORZ) which serve to transport hot reaction products and radicals back to the burner inlet. There the hot reaction products come into contact with fresh gases from the inflow, and the flame is stabilized close to the injector (see for example [3]). The swirl-induced out-of-plane motion is clearly visible, and also impacts the oxidation air jets which create a stagnation zone close to the burner axis after two thirds of the combustor. This additional air splits into a portion flowing towards the exit of the combustion chamber, and part of it is feeding the inner recirculation zone, thereby significantly enhancing the total upstream flow. For operating conditions with combustion this reduces the local equivalence ratio in the inner recirculation zone, creates additional OH and leads to a temperature increase in the lower IRZ, eventually resulting in almost soot-free conditions in parts of

this region [3,4]. Moreover, the tangential velocity component in the inner recirculation zone is reduced by the additional oxidation air.

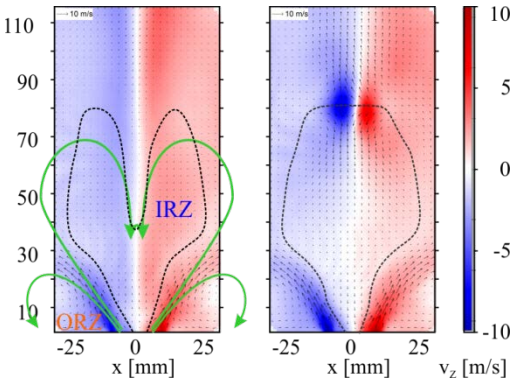

Fig. 1: Mean cold flow field of reference operating point with (right) and without oxidation air (left). The dashed line is the v_y=0 m/s contour.

3.2. Mean Flow Field of Reacting Cases

Qualitatively, the global mean flow field of both reacting cases shows the same characteristics as presented for the cold flow with the main difference of in-flow acceleration past the flame front due to thermal expansion of the mixture (not shown). The fresh flow jets of combustion and oxidation air become wider, and the tangential velocity increases. Widening of the inflow leads to a narrower inner recirculation zone, and the stagnation point, which is inside the central air nozzle for the non-reacting case shifts some millimeters downstream, in accordance with the axial temperature profile presented in [4]. Fig. 2 compares selected velocity profiles obtained with FoV and SoC (for definition see Sect. 2.2) for the rich reference case burning at ϕ=1.2. Both approaches show similar profiles of axial, radial and tangential velocity for the selected profiles, which are dominated by a pronounced back-flow in the inner recirculation zone (top), and a strong out-of-plane motion (bottom). The difference is most evident for the 12-mm profiles (left). Presumably the SoC approach suffers from a bias due to masking part of the images for analysis because of overexposure, while the FoV region more closely resembles that of the leaner flame. The field of view (FoV) profiles are therefore more reliable, and enable a statistical analysis (e.g., RMS) while the information from the sum of correlation analysis (SoC) covers the full combustor, thus provides at least a global qualitative impression when no more detailed information is accessible.

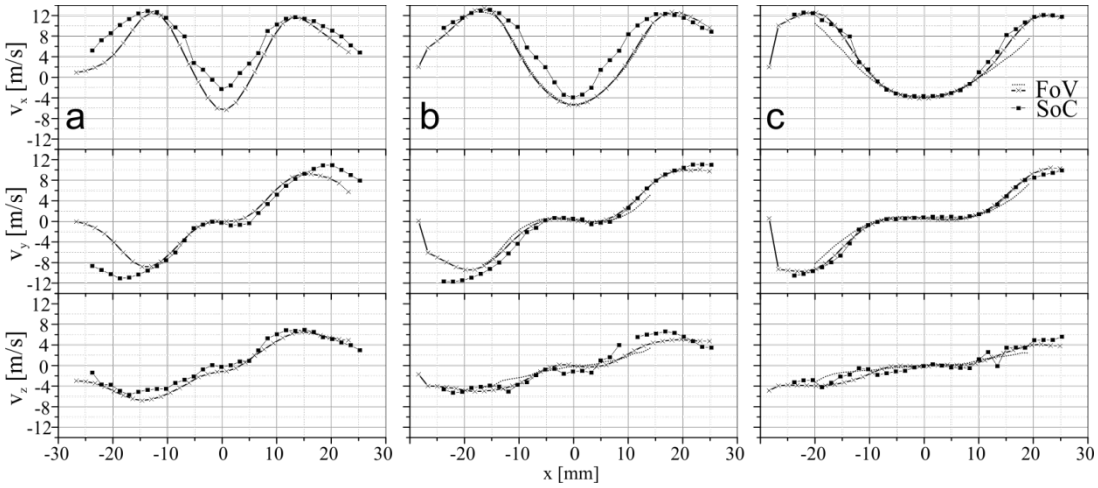

Fig. 2: Axial (top), radial (center), and tangential (bottom) velocity profiles at axial distances of approximately 12 (a), 18 (b) and 24 mm (c), derived from the ϕ=1.2 flame following the sum-of-correlation (SoC, squares) and field-of-view (FoV, thick lines) approach.

3.3. Spatial Correlation of Soot Presence and Mean Flow Field

In recent publications [4,5] the presence of soot in the inner recirculation zone was discussed in relation to the OH distributions, measured by OH LIF. Flame fronts are forming in the inner shear layer (ISL) of the swirling jet between fresh in-flow and hot recirculated reaction products. The relation between the presence of soot and the velocity field is visualized in Fig. 3 for the operating condition at ϕ=0.9. – it is noted that the soot field does not refer to quantitative concentrations but rather is an indication where soot was identified; the fine structure is primarily due to insufficient statistics caused by the high soot intermittency and is not relevant in this context. In the plot, soot is mainly present in the inner recirculation zone. This is qualitatively also valid for the richer test case burning at ϕ=1.2 [5] at higher soot levels. The mean flow field (left) clearly confirms soot presence primarily close to the ISL between in-flow and recirculated reaction products, towards the inner recirculation zone. Here, low to intermediate strain rates prevail (right). There is some overlap of soot presence and regions of globally high in-flow velocities where soot formation is not expected to occur due to the long time scales of soot chemistry [13-15], and of higher mean strain rates. The potential origin of those soot filaments is therefore discussed in the last section which indicates the importance of instantaneous correlations of both quantities.

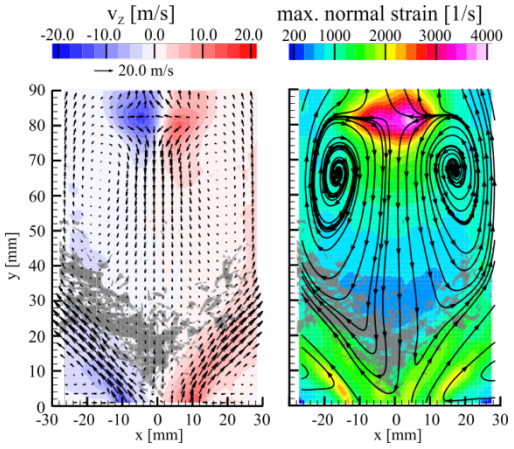

Fig. 3: Soot presence in ϕ=0.9 flame superimposed on a vector representation of the mean flow field (left) and a map of the local extensive strain and stream lines (right). The gray field represents the region of mean soot presence as deduced from laser scattering.

3.4. Effect of Precessing Vortex Core on Flow Field and Soot Distribution

For a more detailed analysis of the relationship between soot and flow-field temporal variations of coherent flow-field structures are taken into consideration. From recent work in this [20,21] and similar burners [23] it is known that a precessing vortex core (PVC) exists in the ISL between the inflow and the IRZ. A dominant, self-excited thermoacoustic oscillation, as identified for other operating conditions (specifically leaner or at different air splits), which can suppress the PVC, [20] was not observed. For the ϕ=1.2 case the PVC frequency was calculated to be about 500 Hz [21]. In the current study, a proper orthogonal decomposition (POD) analysis [22] of 1000 instantaneous velocity fields for the case ϕ=0.9 was performed that confirms the existence of a PVC. The PVC is located in the ISL of the swirling jet where also a major part of soot is present, and therefore an influence of the PVC on soot formation is expected.

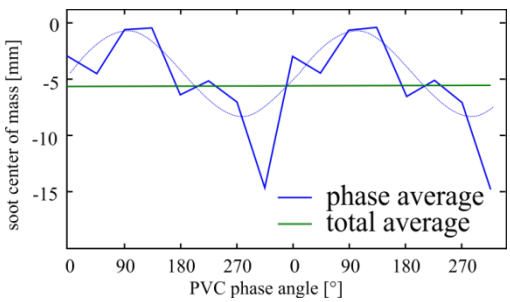

Fig. 4: Variation of the soot center of mass in radial direction with PVC.

For each instantaneous measurement, the phase angle φ of the PVC precession was determined from the respective POD mode coefficients as described in [22], and then phase-conditioned averages of velocity field and soot distribution were calculated for 8 phases (φ=0±22.5°, φ=45±22.5°, etc.). Unfortunately, the correlation between the soot and velocity distributions suffers from a poor soot statistics, even at the relatively large number of 1000 analyzed images. This is due to the relatively low soot load which is a requirement for the applicability of PIV measurements (see Sect. 2.2). Also, the large intermittency of soot appearance [10-12] leads to a relatively low number of images per phase angle with significant soot levels. Fig. 4 depicts the radial motion of the center-of-mass of the soot distribution with phase angle of the PVC; the dashed line serves to guide the eye. This plot is derived by evaluating the eight phase averaged soot distributions, whereof four are displayed in Fig. 5 (top). The slight asymmetry of the soot distributions, which was also identified in [5], results in a non-zero total average of the radial location of the center-of-mass of soot. Despite the relatively poor soot statistics the local influence of the PVC is clearly visible in Fig. 5 which depicts the spatial relation of soot distributions with stream lines and values of extensive strain for four different phase angles of the PVC. The images show that soot is generally present close to the ISL, but soot levels are significantly reduced near the vortices. A detailed interpretation of the soot distributions is difficult based on averaged data due to the transient and history-dependent nature of soot formation. Comparison with PLIF measurements of Ref. [23] suggests that the core of the PVC is characterized by unburnt fresh gas, which prevents soot formation. The same is valid for the outer parts of the PVC vortices adjacent to the in-flowing jets of fresh gas. On the opposite side of the vortices facing the IRZ, frequent soot presence is identified. Therefore the PVC wraps up gases of high hydrocarbon and eventually soot content, which either serves to oxidize soot coming into contact with fresh gases, or to transport soot filaments further upstream towards the stagnation point close to the injector. Close to the PVC compact regions of locally high strain rates are identified, which may be related to suppression of soot formation due to dissipation of the locally rich mixtures [8]. Infrequent occurrence of soot in these regions is therefore probably soot that has been transported here from soot-forming regions in the IRZ. Soot mainly occurs where fresh gases and hot reaction products from the IRZ come into contact, specifically on the hot side of the interaction layer where unburnt hydrocarbons are often present. Taken together, the results confirm the above conjecture that the PVC has a significant influence on soot formation and oxidation, and motivate a more detailed investigation of the mechanisms using enhanced diagnostics.

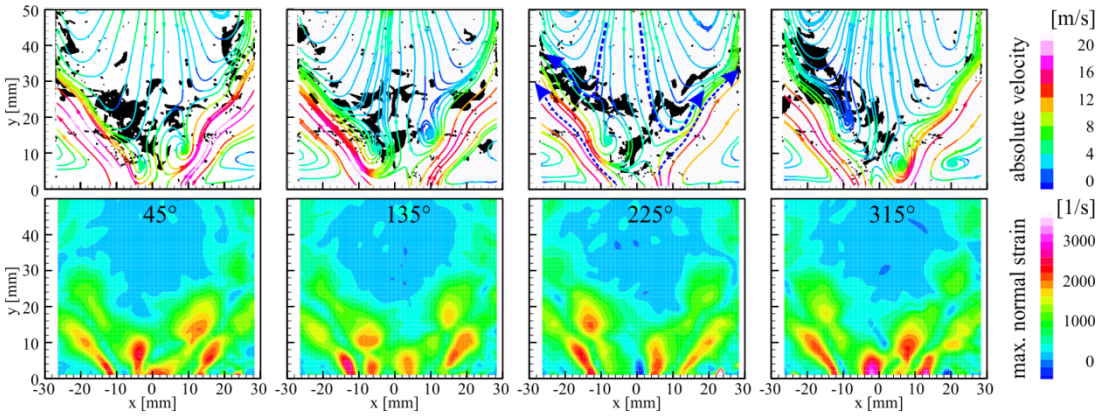

Fig. 5: Phase resolved superposition of soot presence on the flow field in a stream line representation (top), and respective local extensive strain rates (bottom) for four phase angles of the PVC.

3.5. Instantaneous Correlations of Soot and Flow Field

For the understanding of the interaction between flow field and soot formation, the mean flow field is only of limited value, because soot formation strongly depends on the instantaneous fluid structure, temperature and flow condition. Turbulence significantly influences formation of soot, its transport and eventually oxidation. Soot formation in the in-flow region is unlikely due to the relative slow soot formation chemistry on the order of milliseconds; typical instantaneous velocities of the cold in-flow mixture are 15-20 m/s, which relates to propagation distances of at least 20 mm prior to initial soot formation, even if increased temperatures were present at those locations; given typical soot formation times, incipient soot should not be present in the fresh gas in-flow up to at least 20 mm axial distance from the injector. According to Narayanaswamy and Clemens [8] who carefully studied an atmospheric jet flame by LII and PIV, high local strain prevents soot formation. For the ϕ=0.9 flame, presence of soot filaments is correlated to a wide range of local velocities and local extensive strain rates within the whole series of 1000 instantaneous images.

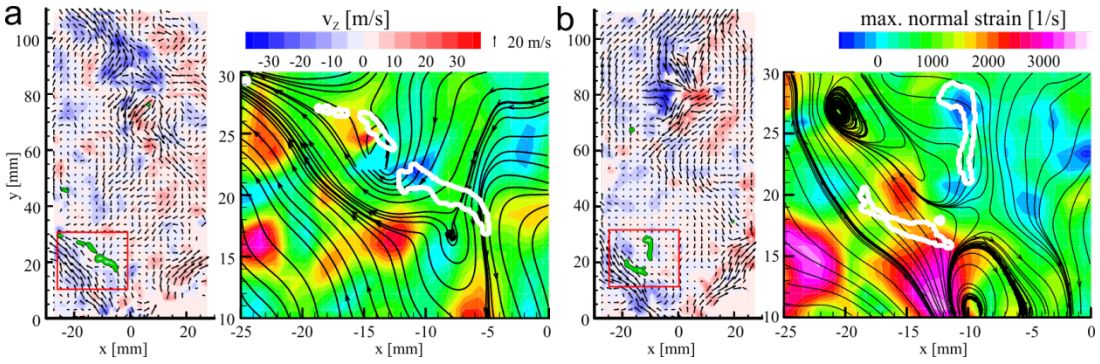

Fig. 6: Two independent exemplary correlations a) and b) of instantaneous soot presence (white contour lines) and flow field and strain rate distribution, respectively. The representations consist of a global flow field (left) and a detailed view (right).

Fig. 6 shows two exemplary correlations of instantaneous flow field and tiny soot filaments, both including a vector representation of the full combustor flow field, and a representation of local extensive strain rates as detailed view. The left plot shows an example of several soot filaments of different typical sizes oriented parallel to the high-velocity in-flow, located a few millimeters towards the inner recirculation zone. The fluid elements have experienced long enough residence times, and here low velocities and low strain rates prevail. The larger filaments are clearly supplied from the inner recirculation zone. Thus conditions are suited for soot

formation and growth. The right example shows two soot filaments, one clearly located in the IRZ characterized by low velocities, and being supplied with hot reaction products from the top. The wider portion of this filament is situated in a region of low strain, the narrower bit is following the stream lines towards the bottom of the image. The second soot filament penetrates into the high-velocity in-flow region which partly exhibits high local strain. Unlike the conditions in jet flames, where regions of soot formation, transport and oxidation can be locally separated, these processes overlap in the complex flow field of a swirl flame. However, it is very likely that soot formation in swirl flames shall predominantly happen at moderate strain rates similar to jet flames as described by Narayanaswamy [8]. They identified a combination of flow velocities of about 3 m/s and strain rates of 700 s^{-1} as preferred conditions for soot formation. Because of that, and the fact that soot formation requires few milliseconds which translates into several 10s of millimeters propagation, this second filament is attributed to transported soot. Most soot filaments within the studied sequence follow these two types of representation. Thus soot found in the high velocity/high strain rate regions in the instantaneous shear layer region is interpreted as transported soot while soot formation regions are located a few mm inside the IRZ where velocities and strain rates are low. As mentioned in the introduction, interpretation of those instantaneous correlations is not straight forward because of the rather long time scale of soot formation. To reveal the history of the soot elements and their interaction with the flow field, a 3D time-resolved simultaneous LII/PIV measurement would be required which is beyond technical possibilities. A correct interpretation of the measured correlations is now and in the near future only possible with the support from numerical simulations. However, time-resolved soot scattering/PIV experiments are planned in future and shall be supportive in bridging the gap of the different time scales.

4. Conclusions

A gas turbine model combustor for partially premixed swirl-stabilized flames was studied with PIV to derive the mean and instantaneous flow fields. These results complement an existing comprehensive data set of pressurized sooting swirl flames, where LII, OH and PAH LIF and CARS were applied. The data consists of flow field information for the cold and reactive flow, in the latter case despite the challenging conditions for PIV measurements caused by strong soot luminosity. For the reference condition at ϕ=1.2 the field-of-view (2-nm interference filtering) and sum-of-correlation (10-nm) approach are in good agreement and complementary in so far as the latter provides the global flow field in the whole combustor while the field-of-

view information serves to deduce statistics. For a leaner test case of ϕ=0.9 which has previously been characterized with respect to soot, OH, PAH distributions and temperature statistics, a detailed study has been performed, which correlates soot presence with the instantaneous flow field. Soot and the distributions of velocities or strain rates do not directly correlate due to the slow soot formation processes which depend on the combination of local composition, residence times of a rich fluid element within this composition and the temperature history. However, making use of knowledge of typical soot formation times, and suitable strain rates for soot formation as identified in literature allows distinguishing between fresh and transported soot. In addition, a precessing vortex core could be identified which prevents soot formation in its center, probably due to lean composition and good mixture, as well as the proximity of compact high-strain regions. Further interpretation of the flow field-soot interaction would require the addition of further simultaneously applied diagnostics such as OH or PAH LIF, preferably with time resolution. With the actual complementation by velocity distributions the full data set is well suited to validate modelers' codes which we encourage by making the data accessible upon request.

Acknowledgement

Part of this work was funded by the European Commission within the Project Fuel Injector Research for Sustainable Transport (FIRST) under Contract No. 265848.

References

[1] M. Mueller, H. Pitsch, Phys. Fluids 25 (2012) 110812.

[2] C. Eberle, T. Blacha, P. Gerlinger, M. Aigner, Proc. 52nd AIAA Aerospace Sciences Meeting 2014, Paper AIAA2014-0132 (2014).

[3] K.P. Geigle, R. Hadef, W. Meier, J. Eng. Gas Turbines Power 136 (2014) 021505.

[4] K.P. Geigle, M. Köhler, W. O'Loughlin, W. Meier, Proc. Combust. Inst. 35 (2015) 3373.

[5] K.P. Geigle, W. O'Loughlin, R. Hadef, W. Meier, Appl. Phys. B 119 (2015) 717-730.

[6] J.H. Kent, S.J. Bastin, Combust. Flame 56 (1984) 29–42.

[7] F. Bisetti, G. Blanquart, M.E. Mueller, H. Pitsch, Combust. Flame 159 (2012) 317-335.

[8] V. Narayanaswamy, N.T. Clemens, Proc. Combust. Inst. 34 (2013) 1455–1463.

[9] A. Coppalle, D. Joyeux, Combust. Flame 96 (1994) 275-285.

[10] N.H. Qamar, Z.T. Alwahabi, Q.N. Chan, G.J. Nathan, D. Roekaerts, K.D. King, Combust. Flame 156 (2009) 1339-1347.

[11] K.P. Geigle, J. Zerbs, M. Köhler, M. Stöhr, W. Meier, J. Eng. Gas Turbines Power 133 (2011) 121503.

[12] V. Raman, R.O. Fox, Annu. Rev. Fluid Mech. 48 (2016) 159–90.

[13] I. Glassman, Proc. Combust. Inst. 22 (1988) 295–311.

[14] M.S. Tsurikov, K.P. Geigle, V. Krüger, Y. Schneider-Kühnle, W. Stricker, R. Lückerath, R. Hadef, M. Aigner, Combust. Sci. Technol. 177 (2005) 1835-1862.

[15] R.D. Lockett, R. Woolley, Combust. Flame 151 (2007) 601-622.

[16] B.M. Cetegen, S. Basu, Combust. Flame 146 (2006) 687–697.

[17] M. Köhler, K.P. Geigle, W. Meier, B.M. Crosland, K.A. Thomson, G.J. Smallwood, Appl. Phys. B 104 (2011) 409-425.

[18] LaVision GmbH, 2011, DaVis 8 Flowmaster Manual.

[19] C. Meinhart, S. Wereley, J. Santiago, ASME J. Fluids Eng. 122 (2000) 285–289.

[20] I. Boxx, K.P. Geigle, C.D. Carter, W. Meier, Proc. AIAA Aerospace Sciences Meeting 2016, Paper AIAA-2016-0435, 2016.

[21] C. Eberle, P. Gerlinger, K.P. Geigle, M. Aigner, Combust. Sci. Technol. 187 (2015) 1841-1866.

[22] M. Stöhr, R. Sadanandan, W. Meier, Exp. Fluids 51 (2011) 1153–1167

[23] M. Stöhr, C.M. Arndt, W. Meier, Proc. Combust. Inst. 35 (2015) 3327-3335.

List of figure captions:

Fig. 1: Mean cold flow field of reference operating point with (right) and without oxidation air (left). The dashed line is the v_y=0 m/s contour.

Fig. 2: Axial (top), radial (center), and tangential (bottom) velocity profiles at axial distances of approximately 12 (a), 18 (b) and 24 mm (c), derived from the ϕ=1.2 flame following the sum-of-correlation (SoC, squares) and field-of-view (FoV, thick lines) approach.

Fig. 3: Soot presence in ϕ=0.9 flame superimposed on a vector representation of the mean flow field (left) and a map of the local extensive strain and stream lines (right). The gray field represents the region of mean soot presence as deduced from laser scattering.

Fig. 4: Variation of the soot center of mass in radial direction with PVC.

Fig. 5: Phase resolved superposition of soot presence on the flow field in a stream line representation (top), and respective local extensive strain rates (bottom) for four phase angles of the PVC.

Fig. 6: Two independent exemplary correlations a) and b) of instantaneous soot presence (contour lines) and flow field and strain rate distribution, respectively. The representations consist of a global flow field (left) and a detailed view (right).

Table

Table 1. Flame parameters for studied flames: Pressure, p, flow rates for air through burner (central and ring), $Q_{air,c}$, and $Q_{air,r}$, fuel, Q_{fuel}, oxidation air through secondary air inlet, Q_{oxi}, equivalence ratios, ϕ, ϕ_{global}, thermal powers, P, P_{global}, and ratios $Q_{air,c}/Q_{air}$ and Q_{oxi}/Q_{air} with $Q_{air}=Q_{air,c}+Q_{air,r}$. Flow rates in standard liters per minute (slm) are referenced to 1.013 bar and 273 K.

p [bar]	ϕ	$P_{primary}$ [kW]	$Q_{air,c}$ [slm]	$Q_{air,r}$ [slm]	Q_{fuel} [slm]	Q_{oxi} [slm]	$\frac{Q_{air,c}}{Q_{air}}$	$\frac{Q_{oxi}}{Q_{air}}$	ϕ_{global}	P_{global} [kW]
3	0.9	32.2	156.0	365.1	32.7	208.2	0.3	0.4	0.64	32.2
3	1.2	32.2	140.8	328.5	39.3	187.4	0.3	0.4	0.86	38.6